

Instrument for studies of homogeneous and heterogeneous ice nucleation in free-falling supercooled water droplets

Stephen E. Wood, Marcia B. Baker, and Brian D. Swanson^{a)}

Department of Earth and Space Sciences, University of Washington, Seattle, Washington 98195

(Received 2 April 2002; accepted 12 August 2002)

We have developed an instrument to study the homogeneous and heterogeneous freezing of droplets in free fall. The advantages of this technique are high repetition rates, telemicroscopic imaging of frozen and unfrozen droplets, and the elimination of possible contamination and nucleation effects induced by substrates. Droplets are ejected at a rate of about 5 per s from a generator at the top of a temperature controlled freezing tube. They fall in a stream down the center of the tube as their images are recorded using video-telemicroscopy. The fraction of drops frozen is measured as a function of height (and, hence, as a function of temperature) by illuminating slices of the stream with linearly polarized laser light and monitoring the depolarization of the backscattered light; ice particles depolarize the scattered light while the liquid droplets do not. The use of depolarization for phase discrimination is unique in this context. We have demonstrated the usefulness of our instrument with pure water droplets and droplets containing water and a bionucleant (*Pseudomonas Syringae*, or "SNOMAX"). The observed homogeneous freezing temperature of pure water droplets is about -37.0°C while heterogeneously frozen water droplets containing SNOMAX freeze at around -8.0°C . We find that the homogeneously frozen pure water droplets tend to be more irregular and bumpy than those heterogeneously frozen. © 2002 American Institute of Physics.

[DOI: 10.1063/1.1511796]

I. INTRODUCTION AND BACKGROUND

Numerical models of the atmosphere show that formation of ice in upper tropospheric clouds can strongly impact cloud dynamics, cloud radiative properties, precipitation formation, and cloud chemistry.¹ It is therefore important to be able to predict the rates of ice formation corresponding to different environmental conditions.

One of the major pathways for ice formation in the atmosphere is through the freezing of supercooled droplets either homogeneously (in the absence of surfaces) or heterogeneously (catalyzed by surfaces). There is now substantial evidence^{2,3} that liquid droplets can persist in the troposphere at temperatures near and below the homogeneous freezing temperature for pure water droplets, $\approx -37^{\circ}\text{C}$. Careful studies of the homogeneous freezing behavior of droplets containing atmospherically relevant organic and inorganic solutes are still needed.

The freezing of droplets in the atmosphere usually occurs at higher temperatures and is heterogeneous, not homogeneous. The nucleating agents can be the surfaces of immersed particles, films at the air-water interface,^{4,5} or partially dissolved materials (for example, low solubility organics) that can go in and out of solution depending on droplet history.⁶⁻⁸ Many laboratory studies of heterogeneous nucleation^{9,10} used AgI as the nucleating agent, but in the absence of a theory of heterogeneous nucleation, it is unclear how to generalize these results to atmospherically relevant

situations. The peculiar ability of some biological materials to promote ice nucleation and others to counteract the formation of ice in metastable aqueous solutions^{11,12} renders them of particular interest in studies of freezing in various geophysical contexts, including atmospheric clouds.

Ice nucleation is not the only important process creating ice particles in clouds. Once some ice has formed by heterogeneous or homogeneous nucleation, secondary processes can multiply the number of existing ice particles.¹³ It has been suggested that splinters formed during freezing of single drops may also serve as embryonic ice particles.¹⁴ The parameters of freezing that lead to droplet deformation and possible splinter production have not been systematically studied. In early studies of drop shattering during freezing, Hobbs and Alkezweeny¹⁴ observed the ejection of splinters from droplets of radii 50–100 μm as they froze in free-fall over a range of temperatures from -20 to -32°C . Application of these interesting results to the atmosphere has been difficult since the statistical samples were relatively small and questions have been raised about the possible effects in early experiments of high laboratory concentrations of CO_2 .¹⁵ Also, we do not have systematic, size, temperature, and humidity dependence of drop shattering or drop deformation preceding shattering over the atmospherically relevant range of droplet sizes.

Several laboratory techniques have been developed to measure ice nucleation rates in small droplets. Summaries of these experiments can be found in several reviews^{9,10} and in the references therein. Among the techniques that have been used are examining freezing of drops on plates, embedding

^{a)}Author to whom correspondence should be addressed; electronic mail: brian@ess.washington.edu

drops in oil emulsions, and using continuous flow diffusion chambers. Some techniques offer the advantages of repeated heating and cooling cycles of the same samples and monitoring the latent heat release during freezing, useful for studies of preactivation and memory effects in heterogeneous freezing. In others, the freezing of cloud drops in air can be observed over a wide range of humidities and temperatures but without detailed examination of individual freezing events.

The new instrument we have developed provides high repetition rate measurements of nearly identical size and composition droplets. Aside from freezing temperature, we also monitor physical properties like changes in droplet shape that often accompany freezing. The supercooled droplets fall in air at terminal velocity which avoids the possible thermal effects and possible contamination caused by substrates. We maintain highly reproducible conditions which allow for the observation of infrequent processes.

In the next section we describe the design and operation procedures of the instrument, and in Sec. III we describe our results for the homogeneous and heterogeneous freezing of droplets with known freezing behavior.

II. INSTRUMENT DESCRIPTION

A. Experimental architecture

The instrument consists of a freezing tube (Fig. 1) which is a vertical hollow brass cylinder about 50 cm in height and 10 cm in diameter. There are two opposing large (plastic) windows, 3.5×26 cm, on the tube sides for observation and illumination of the droplets as they fall. These windows are double-pane and we pass dry nitrogen gas over and between them to prevent frost formation. To cool the tube and establish a vertical temperature gradient, we circulate liquid refrigerant through a pair of copper coils wrapped around the top and base of the tube from a Neslab ULT-80 refrigeration unit. We maintain a temperature inversion (colder at bottom) with a throttle-valve between the two sets of coils. The inversion stabilizes the interior air against convection and helps maintain a stable droplet stream. The tube is insulated on the sides and bottom with foam insulation. On top of the tube is a 2-cm-thick nylon lid with a central cylindrical socket for mounting the droplet generator assembly.

We measure the air temperature inside the tube in the vicinity of the droplet stream with a thermistor attached to the bottom of a glass rod which slides up and down through an off-center hole in the lid. This rod can be rotated to position the thermistor within a few mm of the droplets being observed. A correction factor has been applied to the air temperature measurements to account for the temperature bias due to self-heating of the thermistor and thermal transport down the thermistor wires. The overall temperature gradient in the freezing tube is monitored using four thermistors imbedded in the tube walls. All temperature measurements were made with YSI 44011 precision thermistors calibrated from 0 to -50°C using a NIST-traceable reference PRT thermometer. The total precision and accuracy estimates for air temperature measurements are about $\pm 0.2^\circ\text{C}$ but for our initial experiments we have placed more emphasis on precision than accuracy.

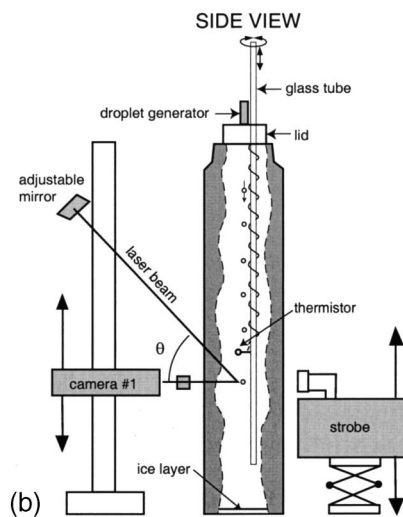
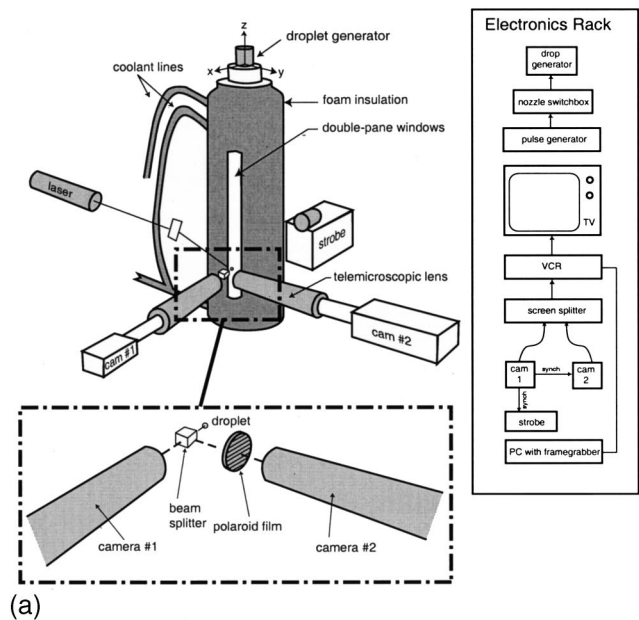


FIG. 1. (a) Schematic diagram of droplet-free-fall apparatus. Droplets are ejected from a droplet generator situated at the top of the cryogenically cooled freezing tube. We use strobe illumination (synchronized to the video frame rate) for imaging the droplets and polarized laser illumination for determination of the fraction of droplets frozen. Two video cameras fitted with telemicroscopic zoom lenses record images or polarized/depolarized light scattering from the falling droplet stream at various heights (corresponding to different droplet temperatures). (b) Side view, showing air temperature measurement thermistor and optics.

B. Droplet generation and characteristics

We generate water droplets using a Hewlett Packard 51604A thermal inkjet print cartridge. Each cartridge has a synthetic rubber bladder, which can hold about 3 ml of water, and there are 12 nozzles on its base that can be fired independently at frequencies of up to 1000 Hz. A nozzle is fired by heating an enclosed resistor with a $4.5 \mu\text{s}$ electrical pulse which vaporizes a small amount of fluid to create a bubble. The growing bubble pushes a droplet out through the nozzle which then breaks off as the bubble collapses. The initial radius ($r_{d,i}$) of the droplets formed by these cartridges is typically about $35 \mu\text{m}$.

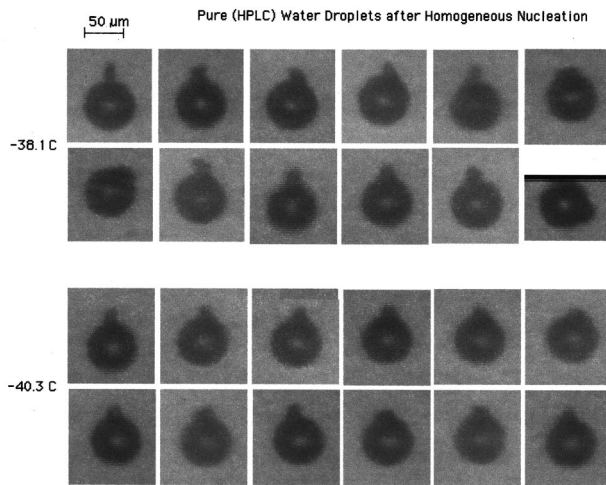


FIG. 2. Representative images of drops just after freezing “homogeneously” at about -37°C from pure HPLC water.

The droplet generation frequency, f_d , is chosen to maximize the number of drops for subsequent statistical analysis while preventing interference between droplets during their fall; if the frequency is too high, a large droplet can catch up with a preceding (smaller) droplet before it reaches the bottom of the tube. This interaction creates instability in the horizontal position of the stream and may allow contact nucleation to occur, thus possibly obscuring the effects of the nucleation process we are trying to study. [Droplet images are shown in Figs. 2 and 3 and instances of these catch up effects are shown in Fig. 3(b).] We estimate the highest allowed droplet generation frequency, $f_{d,\text{max}}$, by setting the average distance between consecutive droplets ($\bar{v}_{\text{term}}/f_{d,\text{max}}$) equal to Δz_{max} , the maximum possible change in the inter-drop distance as two drops of different radii fall to the bottom of the observation window, a distance of length $L = 40$ cm. If v_{term} is the terminal velocity of a drop of radius r_d , then assuming Stokes flow

$$\Delta v_{\text{term}} = 2r_d \Delta r_d \frac{2g}{9\nu} \left(\frac{\rho_d}{\rho_{\text{air}}} - 1 \right), \quad (1)$$

where g is the acceleration of gravity, ν is the kinematic viscosity of air, ρ_d is the density of the droplet, and ρ_{air} is the density of air. Assuming $\Delta v_{\text{term}} \ll \bar{v}_{\text{term}}$, we obtain

$$\frac{1}{f_{\text{max}}} = \Delta v_{\text{term}} \frac{L}{\bar{v}_{\text{term}}^2}. \quad (2)$$

For the HP droplet generator cartridges $\Delta r_d \approx 1 \mu\text{m}$, so for a typical droplet radius of around $33 \mu\text{m}$ ($v_{\text{term}} = 0.13$ m/s), $\Delta v_{\text{term}} \approx 0.007$ m/s, and according to Eq. (2) $f_{\text{max}} \leq 5.5$ Hz in order to prevent droplet interactions as they fall to the bottom of the observation window. This agrees closely with the value we determined by eye, and all of the experimental results presented in this article were obtained using a droplet generation frequency of about 5 Hz.

C. Strobe microscopy and light scattering techniques

Two video charge coupled device cameras with Leica Monozoom-7 zoom lenses are mounted on $x-y$ translation

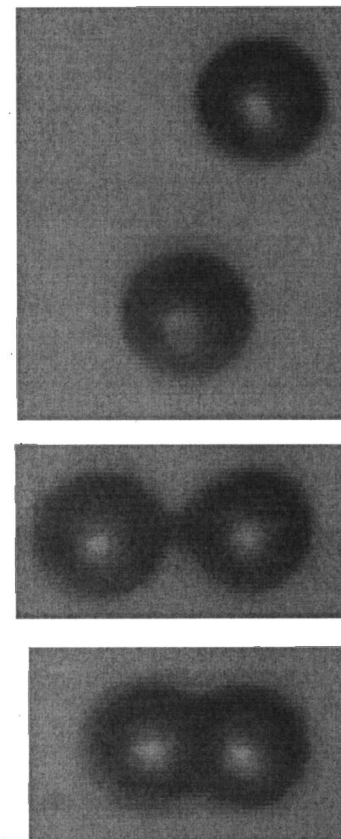
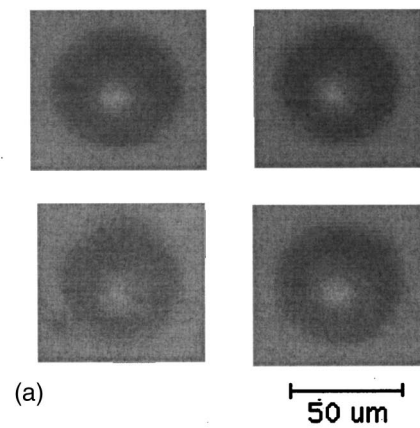


FIG. 3. Representative images of drops just after freezing “heterogeneously” at about -9°C for drops containing bionucleant. (a) Images of droplets during usual low-frequency ($f=5$ Hz) operation. Note the ellipsoidal shape of some droplets. (b) Images of particle deformation and sintering observed during high-frequency ($f=100$ Hz) operation. Sintering was not uncommon when a slightly larger droplet can catch up with a preceding (smaller) droplet.

stages and attached to vertical rack and pinion tracks. These can be positioned and focused for observation of the droplets at any vertical position (z) measured from the floor of the chamber over the length of the front window. The primary camera points directly into the tube and the secondary camera is at a right angle to the primary and observes the droplets through a beamsplitter cube placed between the primary camera lens objective and the front window (see Fig. 1). The video output from the cameras is combined side-by-side us-

ing a video screen splitter and recorded on VHS videotape. Analysis is done with a computer frame grabber converting the video images to 480×640 pixel digital images.

To obtain the backlit “shadow” images of the falling droplets (see Figs. 2 and 3), we illuminate with a diffused xenon strobe lamp placed opposite the primary camera on the other side of the freezing tube. This lamp is raised and lowered to match the camera height. The strobe lamp is synchronized to the video frame rate (60 Hz) of the primary camera. Typical droplets produced by the HP cartridges in our experiment have $r_d = 33 \pm 1 \mu\text{m}$ and $v_{\text{term}} = 13 \pm 0.7 \text{ cm/s}$. The zoom lens configuration we use provides a working distance of 105 mm and a range of magnification from 9.6 to $1.4 \mu\text{m}/\text{pixel}$. The camera field of view at highest magnification ($7\times$) is just 0.07 cm so the chance of capturing an image of each droplet is the ratio of the field-of-view height to the distance the droplet falls between strobe light flashes. At 60 Hz, that distance is $\approx 2.1 \text{ mm}$ for a $33 \mu\text{m}$ radius droplet; so the probability of seeing each droplet at $7\times$ is $0.7 \text{ mm}/2.1 \text{ mm} = 33\%$, and the chance at $1\times$ is 100%. For good image quality the duration of each strobe flash is approximately $1 \mu\text{s}$. In this time interval a typical droplet of radius $r_d = 33 \mu\text{m}$ falls only $0.13 \mu\text{m}$. The primary limitation on image sharpness is the horizontal fluctuation in the position of the droplet stream relative to the camera depth-of-field.

A polarized HeNe laser beam directed through the front window of the freezing tube with an adjustable-tilt mirror is used for ice/liquid discrimination. During an experiment we make two general types of video observations: size and shape observations of droplets as they fall using the strobe lamp and droplet phase determination using laser light illumination. An important design feature of the instrument is the ability to switch from one type of observation to the other without any physical rearrangement of the components. We simply turn off or block whichever light source is not being used.

Droplet phase discrimination. In order to distinguish between frozen and unfrozen droplets, we use the fact that a spherical (liquid) droplet does not depolarize backscattered light whereas a frozen one does due to asphericity in the form of cracks, bumps, and/or surface roughness as well as ice birefringence at short wavelengths. This is the basis for the 180° backscatter depolarization technique used in remote sensing for cloud particle phase discrimination.¹⁶ In the laboratory, depolarization of HeNe laser light scattered at 90° has been used to detect freezing of single droplets levitated in an electrodynamic balance.¹⁷ We are unaware of any previous laboratory instrument utilizing this technique for determining the phase of droplets in free-fall.

We shine a linearly polarized HeNe (633 nm) laser beam on the droplets and direct the approximately 150° backscattered light through a beamsplitter to be imaged by two video telemicroscopic cameras [see Fig. 1(b)]. In front of one camera we have placed a polarizing film oriented perpendicularly to the laser’s direction of polarization. The output signals from each camera are combined using a video screen splitter into side-by-side images (see Fig. 4), and recorded on videotape. The backscattered laser light produces a streak due to

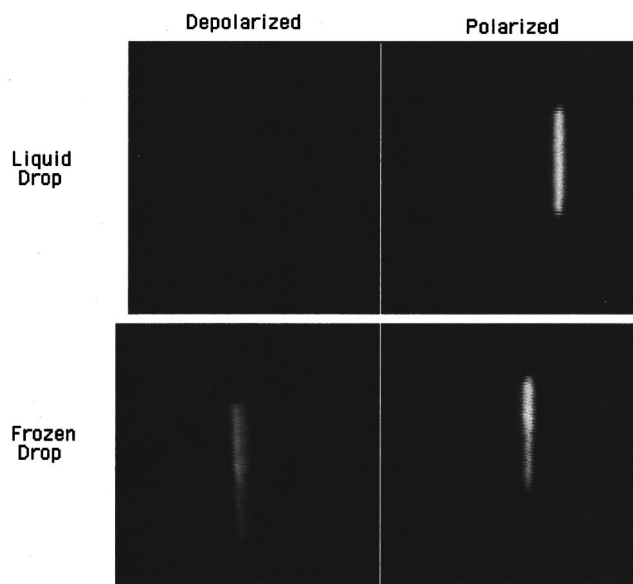


FIG. 4. Streaks showing light backscattered by two falling particles illuminated by polarized laser light. The images on the left show the depolarized component of the scattered light and the images on the right show the component of scattered light of the same polarization as the incident beam. The liquid drop is spherical and therefore does not depolarize scattered light, while the asphericity, surface roughness, and birefringence of the frozen particle contribute to depolarization of scattered light.

the fact that the droplet falls some distance while the camera shutter is open (1 mm in $1/100 \text{ s}$). A liquid droplet produces a streak only on the image made in light of the same polarization as the incident light, whereas a frozen particle produces a streak in both images. To be sure we image the entire length of the streak, we use the lowest zoom magnification for these measurements.

D. Experimental procedure

1. Instrument preparation

Before loading we flush the cartridge reservoir with distilled water to remove any residue from the manufacturing process. The humidity in the freezing tube is adjusted by adding a shallow pool of distilled water at the bottom. Before cooling the tube, we position the air temperature thermistor as close to the droplets as possible and turn on the imaging strobe light. Imaging the thermistor with both cameras enables us to adjust their vertical positions to ensure that each camera will be observing droplets at the same height, namely, that at which the air temperature is measured. This is important in typical temperature gradients of $0.8\text{--}2.4 \text{ }^\circ\text{C}/\text{cm}$. After bringing the droplets themselves into view and focus, we turn off the strobe light and position the laser beam to center the droplet backscatter streak in the field of view. Finally, we orient the directions of the camera polarizers so that none of the copolarized scattered light from the droplets (still at room temperature) can be seen with the secondary camera that views scattering of depolarized light. During the experiment the alignment is occasionally rechecked and adjusted by temporarily swapping the study sample with one that freezes at a lower temperature, such as distilled water or a salt solution.

We used HPLC water for our homogeneous freezing experiments and solutions of HPLC water and the ice nucleant ‘‘SNOMAX’’¹⁸ (commonly used for making artificial snow at ski resorts) for the higher temperature heterogeneous ice initiation experiments. SNOMAX is made from processed cells of the bacterium *Pseudomonas Syringae* (hereafter, PS), one of the most effective ice nucleating agents known. Live cultured cells of PS have been observed to nucleate ice at temperatures as high as -2°C .^{10,22} This bacterium is widespread in nature, found in leaf litter and is a common aerosol/bionucleant in clouds.^{19,20} SNOMAX is manufactured by York Int.¹⁸ using a proprietary process involving freezing at liquid N_2 temperatures and radiation for sterilization purposes. It is packaged in the form of dry pellets about 2 mm in diameter.

In our experiments, one SNOMAX pellet was dissolved in 100 ml of HPLC water and then that solution was filtered through a $0.2\ \mu\text{m}$ syringe filter. This filter size keeps out any intact bacterial cells, which are about $1\times 2\ \mu\text{m}$, and reduces the risk of clogging the droplet generator cartridge nozzles. We have recently found that solutions filtered at sizes up to $5\ \mu\text{m}$ can be used with the HP cartridges, indicating that our instrument can be used for studies of ice nucleation by whole (living) bacterial cells. However, we report only the results for the $0.2\ \mu\text{m}$ filtrate here.

2. Data acquisition

For each data run we record the four tube wall temperatures registered by the embedded thermistors, as well as: (i) droplet sizes [$r_d(z)$], (ii) shapes, (iii) air temperature [$T_{\text{air}}(z)$], and (iv) fraction of drops frozen [$F(z)$] at a range of heights z in the freezing tube. Nucleation is a stochastic process, so not all droplets start to freeze at exactly the same temperature (or height). We refer to the highest point at which any droplets begin to freeze as z_{hi} , and the height at which all droplets have begun freezing as z_{lo} . The freezing process is not instantaneous, but may be slowed by the finite latent heat loss rate. Typical observed values for $\Delta z \equiv z_{\text{hi}} - z_{\text{lo}}$ ranged from 1 to 6 cm depending on the vertical temperature gradient and the nucleant properties. However, it is possible that Δz could be much greater if, for example, only some fraction of the droplets contain a heterogeneous nucleant. In this case two peaks in the frozen fraction would be seen; the first, at relatively high temperature, and the second, at a lower temperature corresponding to those droplets that do not contain nucleant.

If Δz is very small and/or dT/dz is too steep, then it may be difficult to measure points along the $F(z)$ transition curve at the desired resolution by raising or lowering the cameras and thermistor very small distances. An alternative method for obtaining measurements with higher temperature resolution is to keep the cameras and thermistor at a fixed height, and increase or decrease the coolant temperature by small amounts. The main drawback of this method is that it takes more time between measurements because we must wait for the entire freezing tube to come to a new thermal equilibrium rather than just the air temperature sensor.

All camera images are recorded on videotape and marked with a time stamp so that we can later correlate the

video data with the temperature data and other experimental conditions. Typically we record images of the polarized and depolarized laser streaks for about 2 min, giving us a sample of 600 droplets at each temperature.

E. Temperature analysis

In order to compare our nucleation rate observations to theoretical predictions or other experimental data, we must convert our measurements of the air temperature in the vicinity of the droplets into the actual droplet temperature. If the relative humidity is low, droplets evaporate as they fall and their temperature is therefore lower than that of the adjacent air. If the temperature gradient becomes too steep a droplet may not be able to lose heat fast enough to keep up and will become warmer than the air it falls through. In order to calculate these effects we use a simple numerical model (described in the Appendix) for the evolution of the temperature and radius of water droplets as they fall through air with given vertical profiles of temperature and relative humidity.

F. Image and depolarization analysis

We record both the laser streak images and the strobe-lit droplet images on videotape at approximately one streak or image for every ten video frames. To analyze the data we use a data analysis program (NIH Image) and computer connected via an RS-232 interface to the VCR to automatically identify and archive the video frames containing droplet images. The computer advances the videotape one frame at a time and each image is captured and digitized with the frame grabber card. We collect 300–600 droplet streaks for each temperature value, and bin the images in 5 s intervals, giving us from 12 to 24 bins each containing 25 droplets. We then simply count the number of polarized and depolarized streaks. [Because the depolarized streaks can be quite faint, this is done manually using appropriate background intensity threshold settings. Typically this can be done at a rate of about 1 frame/s and even at low intensity levels, the characteristic shape and position of the depolarization streak usually make identification of frozen versus unfrozen droplets quite straightforward (less than 1% of the frames are ambiguous). The automation is important to the most time-intensive portion of the analysis which is the initial finding of the frames with the polarized/depolarized streaks.] Finally, we calculate the average value and standard deviation of frozen fraction $F(T)$ for all of the bins at a particular height (temperature).

We obtain strobe images of the falling droplets at both the highest ($7\times$) and lowest ($1\times$) zoom magnifications to characterize the droplet shape, size, and fall distance. Measurements of droplet size from $7\times$ images can be made directly, but the size obtained from fall distance measurements is more precise because the terminal velocity depends on the square of the droplet radius; a $35\ \mu\text{m}$ radius droplet falls 2.32 mm in $1/60\ \text{s}$ which, at the $1\times$ image resolution of $9.6\ \mu\text{m}/\text{pixel}$, equals 242 pixels, or about half of the field of view. A droplet whose diameter is larger by $1.4\ \mu\text{m}$ (the resolution limit at $7\times$) would fall 250 pixels in $1/60\ \text{s}$. Because we can measure the fall distance to within 1 pixel in

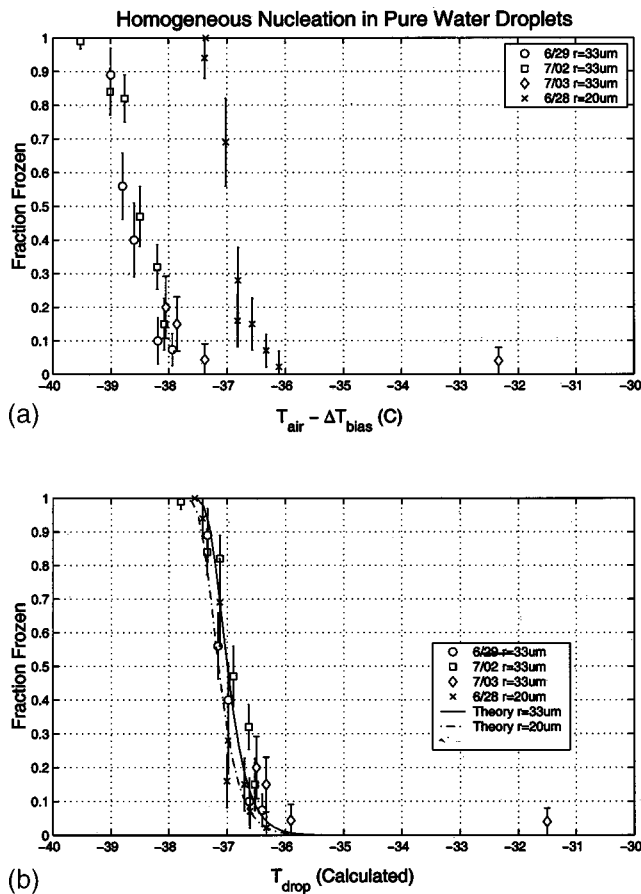


FIG. 5. HPLC water droplets. (a) Fraction of HPLC droplets frozen vs estimated local air temperature, which is the measured air temperature minus the estimated warm bias of the thermistor. The different symbol types correspond to datasets obtained on four different days, and different drop sizes. (b) Same results replotted as a function of model-calculated droplet temperature. Solid line: fit to previous data from Ref. 21.

$1 \times$ images, this method has a precision of about $0.2 \mu m$ for the size range of droplets in our experiments ($r_d = 20-35 \mu m$).

III. RESULTS

A. Freezing temperatures

Homogeneous freezing: HPLC droplets. The experiments were performed for two different final droplet sizes: $r_d = 33$ and $20 \mu m$, where final refers to the size when freezing occurred. Figure 5 shows F for frozen HPLC droplets for a range of temperatures corresponding to different heights in our droplet tube. The upper panel shows the data plotted versus air temperature. The droplets can be either colder or warmer than the surrounding air due to (i) latent heating or cooling during growth or evaporation, and to (ii) the inability of larger droplets to keep up with rapid cooling rates. We have used our model (see the Appendix) to compute the difference between droplet and air temperature, and the bottom panel of Fig. 5 shows we get good agreement between data runs once the correction is included. We find that most droplets freeze over the temperature range from -36 to $-38 \text{ }^\circ\text{C}$ with a small dependence on the droplet size. At these temperatures, the effect of evaporative cooling is negligible, but

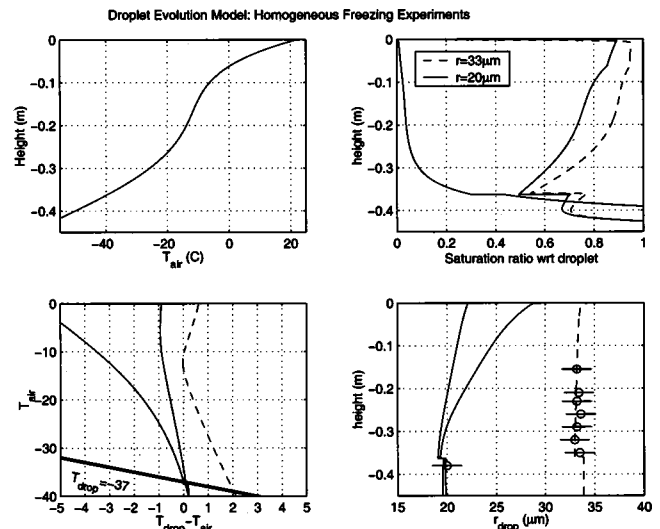


FIG. 6. Model calculation results (see the Appendix) used to obtain the actual droplet temperature for the homogeneous freezing case using the measured $T_{air}(z)$ and $r_d(z)$. Upper left panel: measured (with bias correction) air temperature $T_{air}(z)$ along the droplet stream. Lower right panel: measured droplet radius $r_d(z)$ and the resulting saturation ratio model fits. Upper right panel: Two saturation ratio models (wet walls and dry walls) for the $r = 20 \mu m$ case and one model (dry walls) for the $r = 33 \mu m$ case. These results were obtained by fitting f_{hum} [Eq. (A4)] so that model predictions match the measurements of $T_{air}(z)$ and $r_d(z)$. Note that the kink occurs at the freezing point. Lower left panel: the actual droplet temperature $T_{drop}(z)$ expressed as an offset from $T_{air}(z)$. Typically we measure $r_{drop}(z)$ at many positions along the stream but in the $r = 20 \mu m$ case we see that at the freezing temperature ($-37 \text{ }^\circ\text{C}$) both saturation ratio models give nearly the same offset.

the thermal lag effect can be significant due to the steep temperature gradient (2.4 deg/cm) used in these experiments. Our model calculations (see Fig. 6) show that $33 \mu m$ droplets are $2 \text{ }^\circ\text{C}$ warmer than the air temperature at the freezing level, whereas the smaller $20 \mu m$ radius droplets are at the same temperature within $0.1 \text{ }^\circ\text{C}$. The maximum temperature difference inside a droplet ($T_{center} - T_{surface}$) was always less than about $0.15 \text{ }^\circ\text{C}$ which we have ignored since we do not know where inside the droplet the freezing starts. In Fig. 7 is

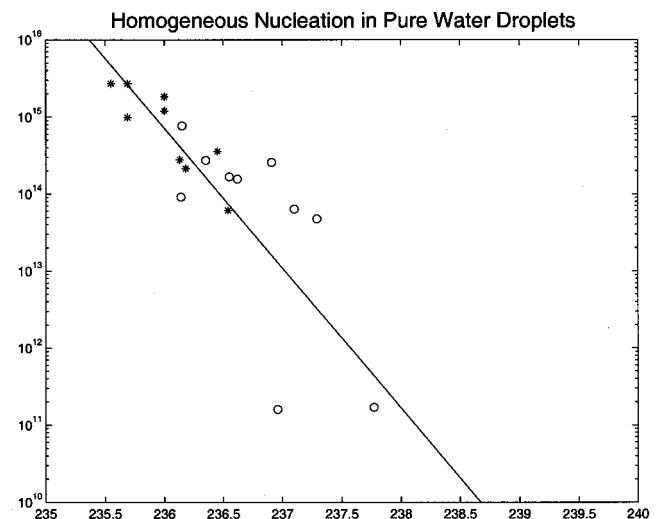


FIG. 7. Same data as Fig. 5, replotted as freezing rate J . Circles: $r_d = 20 \mu m$; *, $r_d = 33 \mu m$. Fit to previous data (Ref. 21) shown as a line.

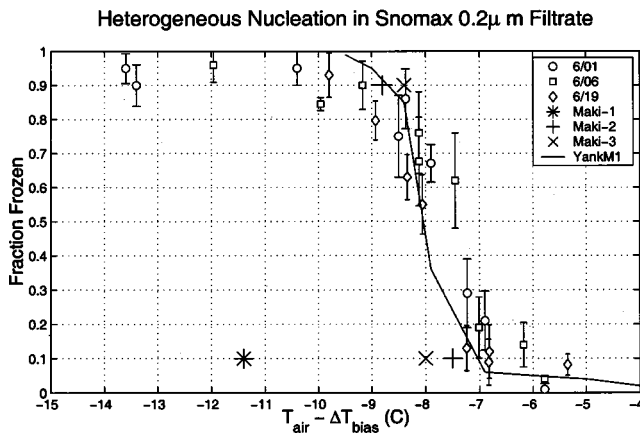


FIG. 8. Measured frozen fraction vs temperature for heterogeneously frozen droplets containing the bionucleant SNOMAX. The three sets of measurements were made on three different days (different small symbols with error bars). The previous measurements of the nucleation rates for whole and fragmented PS cells (large symbols) are shown for comparison (Ref. 22). The solid line is a freezing spectrum of the $0.45 \mu\text{m}$ filtrate of a different INA bacterium (M1) after sonic disruption of the cells (Ref. 30).

plotted the HPLC data (points) and the previous nucleation rate data (line) tabulated by Pruppacher;²¹ the fit for drops of volume $V_d[\text{m}^3]$, cooling rate \dot{T} experienced by the drops is given by

$$J[\text{m}^{-3} \text{s}^{-1}](T) = 10^{(6 - 1.8154T - 58.589)}, \quad (3)$$

$$F(T) = 1 - \exp\left[-V_d/\dot{T} \int_0^T J(T)dT\right], \quad (4)$$

where here T , the droplet temperature, is measured in centigrade. We note that the mean homogeneous freezing temperature and distribution width are in good agreement with the previous nucleation rate data.

B. Heterogeneous freezing: SNOMAX containing droplets

Figure 8 shows the freezing data for the SNOMAX droplets. For these droplets, we observe no significant evaporation during their fall, and for the shallower temperature gradients in these experiments, our model calculations show that there would be very little thermal lag even for the largest droplets studied. (We estimate at saturation the thermal lag is about 0.4°C and is smaller for evaporating droplets.) As is shown in Fig. 8, most of the drops freeze over the temperature interval $-10 \leq T_f \leq -6^\circ\text{C}$. These results compare quite well with those of Maki *et al.*²² on unfiltered, disrupted cells, but not with their $0.45 \mu\text{m}$ filtrate results, where they found freezing began about 1.4°C colder than ours. Liao and Ng²³ report results close to ours for nucleant concentrations given as $300 \text{ g}/100 \text{ kgal}$ ($0.8 \text{ mg}/\text{l}$), in droplets about $50 \mu\text{m}$ in diameter. (The weight percent of our solutions are about $0.1 \text{ g}/\text{l}$.) Our nucleating agent must be smaller in size than $0.2 \mu\text{m}$; thus we are finding considerable nucleating ability apparently not associated directly with the larger PS bodies themselves.

In order to easily compare the homogeneous and heterogeneous freezing data sets we have fit the frozen fraction $F(T)$ data to the error function parameterization

$$F(T) = 1/2\{1 + \text{erf}[(T_{f0} - T)/\sigma]\} \quad (5)$$

with two free parameters to extract quantitative estimates of the freezing initiation temperature and standard deviation of the freezing temperature distribution. The best fit temperatures are $T_{f0} = -6.7^\circ\text{C}$, standard deviation $\sigma = 2.5^\circ\text{C}$ for the heterogeneous case and initiation freezing temperature $T_{f0} = -36.5^\circ\text{C}$, standard deviation $\sigma = 1.0^\circ\text{C}$ for the homogeneous case. The width of the heterogeneous freezing temperature distribution is much broader than the homogeneous distribution and may reflect variability in the heterogeneous nucleant concentration in the drops, variability in the location of the bacteria and their excreta within the drops, as well as possible variation in energies of freezing sites on each nucleator.

C. Shapes of frozen particles

A number of previous authors^{24,25} have obtained images of frozen water drops and noted protuberances, bulges (spicules), and signs of drop shattering. However, these were images of larger drops and generally drops that froze on a substrate. With our new instrumentation we have the capability of observing hundreds of frozen droplets in air to categorize the various shapes upon freezing. Figure 2 shows a representative set of images (for $T_{\text{drop}} \sim -38$ and -40°C ; i.e., well after the onset of freezing) of homogeneously frozen pure water drops taken at high magnification ($1.4 \mu\text{m}/\text{pixel}$). Most of the droplets display bulges, or hook-like structures. For this set of 24 representative droplets with bulges with average frozen droplet diameter $46 \mu\text{m}$ the average bulge height is $10 \pm 4 \mu\text{m}$. From 200 sequential frozen droplet images, we find at least 86% of the droplets have bulges or spicules larger than $3 \mu\text{m}$ high. Nearly all droplets appear to orient with the bulges “up” but since bulges in other orientations are difficult to detect in the images, the percentage of droplets with bulges could be larger.

A similar analysis of a representative set of high-resolution images (a few are shown in Fig. 3) of frozen (known from the depolarization signal) SNOMAX droplets show very few bulges or deformations larger than $1 \mu\text{m}$. In this case, the vast majority of heterogeneously frozen droplets maintain nearly spherical shapes, many more than are observed in the homogeneously frozen case.

IV. DISCUSSION

In these preliminary measurements, we find this instrument works well and is useful for studying ice nucleation in supercooled droplets in free-fall over a wide range of temperatures. (Although not reported here, we have performed freezing experiments with ionic solutions at temperatures as low as -50°C , also with reproducible results.) The freezing rate results we obtained for pure water and SNOMAX are consistent with previous work and we are able to analyze the images of the drops prior and post freezing. Although we are unable to determine precisely how much time has elapsed after freezing for each image, the fact that our mean freezing temperatures, recorded via the depolarization signal, are close to the freezing temperatures reported by previous au-

thors, indicate that the depolarization signal is measurable well within a few seconds after freezing. The perturbations in optical parameters in newly frozen droplets are sufficiently large that they may modify the light scattering properties of the particles in an important way, an issue that deserves further attention.

The early deformations are characterizable and appear to depend on freezing temperature (i.e., in our experiments, on freezing mode). Bumps are more common in the HPLC droplets. This is likely because they can freeze more completely in the initial stage before the droplet warms up to 273 K so that it is more likely water will get squirted out by the pressure buildup. The droplets tend to orient in the airstream such that the bumps are on top, probably because of drag. The few which are not on top could have been photographed just after formation before the frozen particle had had time to reorient. Ice particles nucleated on SNOMAX at relatively high temperatures seem to be more ellipsoidal than those that froze homogeneously. It is not clear what causes this difference; it might reflect differences already apparent in the liquid drops prior to freezing or it may indicate something about the freezing mode. Observations of later stage growth of both heterogeneous and homogeneously frozen droplets show that these initial deformities appear to disappear after about a $2\times$ increase in size but droplets frozen at colder temperatures tend to produce more polycrystalline particles.²⁶

Although many frozen particles in this study exhibited bumps or spicules, we did not observe instances of breakup or the production of satellite droplets associated with droplet distortion and spicule formation. The small size of the droplets in this study makes these processes unlikely and such short-lived processes would in any case be difficult to capture photographically at standard video frame rates given our current illumination configuration.

For some future experiments there are several features of the instrument and protocol that we plan to modify. We are concerned that the droplet generator ejects droplets at a high (and unknown) temperature. The droplets cool down quickly, and our results from the bionucleant studies showed freezing temperatures similar to those observed in previous substrate studies with unheated samples, but the heating process may affect other bionucleants. An additional concern is that the droplets are ejected at high velocity ($v_{d,i} \approx 10$ m/s according to HP specifications), whereas the terminal velocity (v_{term}) of a $35 \mu\text{m}$ radius droplet is ≈ 14 cm/s.²⁷ We estimate the deceleration time to be less than 0.05 s, and the deceleration distance to be less than 5 cm, using empirical drag coefficients for $\text{Re} > 1$.⁹ The most conservative estimate of droplet cooling time, assuming $T_{d,i} = 100^\circ\text{C}$ and $v = v_{\text{term}}$, is 0.1 s. This can be problematic for heterogeneous systems that freeze at warmer temperatures if the freezing process is slowed down by kinetic processes in the droplet. We plan to remove these uncertainties by developing new droplet-on-demand systems using microvalves or piezoelectric droplet generators to produce nonheated and slower emitted droplets. Finally, to speed up our data analysis techniques, we plan to explore the use of photodiodes or photomultipliers in

place of the camera images to automatically measure the frozen fraction in real time.

ACKNOWLEDGMENTS

The authors thank Leo Shen and Andy Mason at the Hewlett Packard Corporation for supplying the inkjet cartridges, and Wayne Palmiter at York International for providing samples of SNOMAX. The authors also thank Bryan Venema for assistance in building the pulse generator electronics for the inkjet cartridges; Brian Majeres, Tim Whitcomb, and Robert Seguin for help with the experiment; and Neil Bacon for helpful experimental suggestions. Support for this research was provided by NSF Grant No. ATM-9906538.

APPENDIX: NUMERICAL MODEL FOR FALLING DROPLET EVOLUTION

We use a standard Maxwell-type model to calculate the temperature and radius of a water droplet as it falls through the temperature and humidity gradient in the freezing tube. The model is similar to that of Hobbs and Alkezweeny,¹⁴ but we have included droplet evaporation, which can be important for our case. For simplicity, the droplet is always assumed to be falling at its terminal velocity. This assumption is reasonable because the ejected droplets slow to terminal velocity after a few cm and well before the height at which we make our measurements. The range of Reynolds numbers for droplets in our experiments was 0.2–1.1, so that we may use the Oseen drag coefficient,⁹ $C_d = (24/\text{Re}) * [1 + (3 * \text{Re}/16)]$.

We neglect droplet–droplet interactions in the flux calculations because, first, the distance between drops is much larger than the droplet radius ($v_{\text{term}}/f_{\text{max}} \approx 0.2 * 0.1 = 0.02$ m $\gg r_d$), and second, the time scale for relaxation of the diffusive gradients around each drop is much faster than the droplet generation rate ($\tau_{\text{diff}} \approx 3 * 10^{-5}$ s (for $r = 25 \mu\text{m}$) $\ll 1/f = 1/5$ Hz = 0.2 s), so there is plenty of time for the gradients around the droplet at a given position to dissipate before the next droplet arrives.

Thus we have for the mass and heat flux

$$F_m = f_v \frac{D_v}{(R_v r_d)} \left[\frac{e_{\text{eq}}(T_{\text{drop}})}{T_{\text{drop}}} - \frac{e(z)}{T_{\text{air}}(z)} \right], \quad (\text{A1})$$

$$F_q = f_v * \kappa_{th} / r_d * [T_{\text{drop}} - T_{\text{air}}(z)], \quad (\text{A2})$$

where $f_v = 1.0 + 0.108 * [(\eta/D_v)^{1/3} * (\text{Re}^{1/2})]^2$ is the ventilation coefficient,⁹ which was never greater than 1.07 for the droplets in our experiments ($\text{Re} \leq 1.1$).

We solve for the unknown droplet temperature (T_{drop}) iteratively using conservation of energy,

$$F_q = -F_m * L_e [T_{\text{air}}(z)] \quad (\text{A3})$$

and the latent heat of evaporation is $L_e(T) = 597.3 * (273.15/T)^{(0.167 + 3.67 * 10^{-4} * T)} * (1000/0.2388) \times [\text{J/kg}]$.⁹ The vapor pressure of supercooled liquid water is calculated using a sixth-order polynomial equation from Lowe and Ficke.²⁸ The temperature dependent heat capacity

of supercooled liquid water is $c_p(T_{\text{drop}}) = -0.0303 * T_{\text{drop}}^3 + 24.73 * T_{\text{drop}}^2 - 6740 * T_{\text{drop}} + 617\,600$, T_{drop} in Kelvin.²⁹

Due to the difficulty of measuring the humidity profile in the chamber, we treat the humidity as an adjustable parameter in the model and find the value which gives the best fit to the observed values of droplet size as a function of height, $r_d(z)$. Using this model fit, we can then create a function relating the measured air temperature values to the corresponding droplet temperatures.

If the range of droplet freezing temperatures is low enough, evaporative cooling is negligible for any humidity and the model is only needed for calculating the thermal lag effect. For all other cases, we vary the model humidity profile between the wettest and driest possible conditions. The wettest is the case when the inner walls of the freezing tube are coated with water or ice; in this case $e_{\text{max}}(z) = e_{\text{eq}}[T_{\text{wall}}(z)]$, the equilibrium vapor pressure of water or ice at the temperature of the wall at that height. The driest possible profile is that obtained if the only source of water vapor is the ice layer at the bottom of the tube, so that $e_{\text{min}}(z) = e_{\text{eq}}(T_B)$.

The model profile is adjusted using a single parameter f_{hum} , such that

$$e(z) = e_{\text{min}}(z) + f_{\text{hum}}[e_{\text{max}}(z) - e_{\text{min}}(z)]. \quad (\text{A4})$$

¹L. Fowler and D. Randall, *J. Clim.* **9**, 561 (1996).

²A. Heymsfield and L. Miloshevich, *J. Atmos. Sci.* **50**, 2335 (1993).

³D. Rosenfeld and W. Woodley, *Nature (London)* **405**, 440 (2000).

⁴M. Gavish, R. Popovitz-Biro, M. Lahav, and L. Leiserowitz, *Science* **250**, 973 (1990).

⁵R. J. Davey *et al.*, *Langmuir* **10**, 1673 (1994).

⁶B. Zuberi, A. Bertram, T. Koop, L. T. Molina, and M. J. Molina, *J. Phys. Chem. A* **105**, 6458 (2001).

⁷T. Tabazadeh and O. Toon, *Geophys. Res. Lett.* **25**, 1379 (1998).

⁸M. B. Baker, *Nature (London)* **413**, 586 (2001).

⁹H. R. Pruppacher and J. D. Klett, *Microphysics of Clouds and Precipitation* (Reidel, Dordrecht, 1978).

¹⁰G. Vali, Ice Nucleation-Theory: A Tutorial, Presented at the NCAR/ASP 1999 Summer Colloquium (unpublished).

¹¹K. E. Zachariassen and E. Kristiansen, *Cryobiology* **41**, 257 (2000).

¹²C. A. Knight, *Nature (London)* **406**, 249 (2000).

¹³S. C. Mossop, *Bull. Am. Meteorol. Soc.* **66**, 264 (1985).

¹⁴P. Hobbs and A. Alkezweeny, *J. Atmos. Sci.* **25**, 881 (1968).

¹⁵J. E. Dye and P. V. Hobbs, *Nature (London)* **200**, 464 (1966).

¹⁶K. Sassen, in *Light Scattering by Nonspherical Particles: Theory, Measurements, and Applications*, edited by M. I. Mishchenko, J. W. Hovenier, and L. D. Travis (Academic, New York, 2000), pp. 393–403.

¹⁷B. Kramer, O. Hubner, H. Vortisch, L. Woste, T. Leisner, M. Schwell, E. Ruhl, and H. Baumgartel, *J. Chem. Phys.* **111**, 6521 (1999).

¹⁸York International, Victor, New York, 14564.

¹⁹D. C. Sands, V. E. Langhans, A. L. Scharen, and G. DeSmet, *Időjárás* **86**, 148 (1982).

²⁰H. A. Constantinidou, S. S. Hirano, L. S. Baker, and C. D. Upper, *Phytopathology* **80**, 934 (1990).

²¹H. R. Pruppacher, *J. Atmos. Sci.* **52**, 1924 (1995).

²²L. R. Maki, E. L. Galyan, M. Chang-Chien, and D. R. Caldwell, *Appl. Microbiology* **28**, 456 (1974).

²³J. C. Liao and K. C. Ng, *Ind. Eng. Chem. Res.* **29**, 361 (1990).

²⁴D. A. Johnson and J. Hallett, *Q. J. R. Meteorol. Soc.* **90**, 468 (1964).

²⁵R. L. Pitter and H. R. Pruppacher, *Q. J. R. Meteorol. Soc.* **99**, 540 (1973).

²⁶N. J. Bacon, M. B. Baker, and B. D. Swanson, *Q. J. R. Meteorol. Soc.* (to be published).

²⁷These calculations were performed for initial 300 K droplets in air at 100 kPa, corresponding to the typical conditions at the top of a freezing tube.

²⁸P. R. Lowe and J. M. Fick, Tech. Paper No. 4-74, Environmental Prediction Research Facility, Naval Postgraduate School, Monterey, CA, 1974.

²⁹C. A. Jeffery and P. H. Austin, *J. Geophys. Res.* **102**, 25269 (1997).

³⁰S. A. Yankofsky *et al.*, *J. Appl. Meteorol.* **20**, 1013 (1981).